

1
2
3
4
5
6
7
8
9
10
11
12
13
14
15
16
17
18
19
20
21
22
23
24
25
26
27
28
29
30

Geophysical Research Letters

Supporting Information for

Precession-paced inter-gyre connectivity and northward heat transport to northeastern North Atlantic during the Mid-Pleistocene Transition

M. Carolina A. Catunda^{1*}, André Bahr¹, Stefanie Kaboth-Bahr^{2,1}, Xu Zhang^{3,4}, Nicholas P. Foukal⁵, Oliver Friedrich¹

¹Institute of Earth Sciences, Heidelberg University, Im Neuenheimer Feld 234–236, 69120 Heidelberg, Germany.

²Institute of Geosciences, University of Potsdam, Karl-Liebknecht-Straße 24–26, 14476 Potsdam-Golm, Germany.

³College of Earth and Environmental Science, Lanzhou University, Tianshui S. Road 222, Lanzhou, 730000, China

⁴Alfred Wegener Institute Helmholtz Center for Polar and Marine Research, Bussestr. 24, Bremerhaven, D-27570, Germany

⁵Department of Physical Oceanography, Woods Hole Oceanographic Institution, Woods Hole, MA, USA.

*Corresponding author: M. C. A. Catunda (carolina.catunda@geow.uni-heidelberg.de)

Contents of this file

Text S1 to S6
Figures S1 to S9
Table S1

31 Introduction

32 The supporting information includes the description of methods used for the age
33 model update of U1313, more details regarding the choice of oceanographic database,
34 supporting data regarding the relationship between dryness in Eastern Mediterranean and
35 methods used for the modelling section discussed in the main text. Supporting figures
36 detail points made and are cited along the main text. Table S1 provides all tie points
37 between LR04 and Site U1313 on the amcd depth scale.

38

39 S1. Oceanographic dataset, figures and inferences

40 All oceanographic figures were prepared using the software Ocean Data View
41 (*Schlitzer, 2002*) and data from the World Ocean Atlas 2018 (*Locarnini et al., 2019; Zweng*
42 *et al., 2019*). Water masses above the studied site were defined according to their potential
43 temperature and salinity characteristics (Figure S2).

44 At 800m water depth above Site U1313, the water column is characterized primarily
45 by Subpolar Mode Water of 8°C, SPMW₈ (*Brambilla et al., 2008; García-Ibáñez et al., 2018*),
46 that carries the thermohaline properties of the Iceland Basin close to Rockall Trough. There
47 has been a lot of discussion about the degree of MOW's heat and salinity contribution to
48 the characteristics of SPMW, and by extension the eastern SPG and Atlantic inflow into the
49 Nordic Seas (*Reid, 1979; Harvey, 1982; McCartney and Mauritzen, 2001; Lozier and Stewart,*
50 *2008*). Such assessment is not trivial because temperature-salinity relationships close to
51 the Rockall Trough are complex (*Pollard et al., 1996*) and variable on short timescales,
52 leading to different conclusions dependent on the analyzed dataset (*Lozier and Stewart,*
53 *2008*). Given the very long timescales of this study, we disregard decadal variability by
54 using data from the World Ocean Atlas 2018, that provides time integrated data from over
55 15 million stations measured between 1955 and 2018 (*Locarnini et al., 2019; Zweng et al.,*
56 *2019*). Although this dataset is biased towards the more recent decades (because of higher
57 volume of available data), it is the best dataset available for time integrated analysis of the
58 modern hydrography of the North Atlantic. Figure 1, in the main text, shows temperature
59 and salinity distribution for the isopycnal level at 800m water depth above Site U1313 (σ_0
60 = 27.45). Temperature and salinity at this density level covary and radiate from the Gulf of
61 Cadiz, leaving little doubt that MOW modulates temperature distribution at the dwelling
62 depth of *G. crassaformis* in the subtropical North Atlantic.

63 At 800 m water depth, the dwelling depth of *G. crassaformis* at Site U1313 also
64 coincides with the top of the pycnocline, where the high vertical density gradient leads to
65 the accumulation of organic matter fallen from the surface. Cléroux et al. (2013) suggests
66 that the preference of *G. crassaformis* for these conditions may be due to the abundance
67 of food and lower predational pressure of low-oxygen environments.

68

69 **S2. Update of Site U1313 age model**

70 For this study, we revised the previously published Site U1313 stratigraphy for the
71 time interval between MIS 36 and MIS 14 (Naafs et al., 2012). In particular, we generated
72 290 new benthic stable oxygen isotope data points based on *Cibicidoides wuellerstorfi* and
73 *Uvigerina peregrina* from the primary splice for the interval 1203–543 ka, improving the
74 low-resolution benthic isotope records by (Naafs et al., 2011, Figure S3).

75 Stable oxygen isotope ratios were measured on a Thermo Fischer MAT 253 Plus
76 IRMS gas isotope ratio mass spectrometer with coupled Kiel IV automated carbonate
77 preparation device at the Institute for Earth Sciences at Heidelberg University. The
78 instrument was calibrated using the in-house standard (Solnhofen limestone), itself
79 calibrated against the IAEA-603. The standard deviations (reproducibility) for repeated
80 measurements of the in-house standard were 0.08‰ for $\delta^{18}\text{O}$. The analyses results were
81 normalized according to Paul et al. (2007). The standard deviations (reproducibility; n=10)
82 for repeated sample measurements were also 0.08‰ for $\delta^{18}\text{O}$. To allow for a continuous
83 record comprising data of both species, $\delta^{18}\text{O}$ values of *Cibicidoides wuellerstorfi* were
84 corrected to bottom-water $\delta^{18}\text{O}$ values by adding 0.64‰ (Shackleton and Opdyke, 1973).
85 For depth-age conversion we tuned the combined and species-adjusted benthic $\delta^{18}\text{O}$
86 record of Site U1313 to the LR04 benthic stack (Lisiecki and Raymo, 2005) using the
87 software AnalySeries 2.0.8 (Paillard et al., 2011). All tie points used are listed in Table S1.

88

89 **S3. Potential sources of errors affecting the discussed proxy records and**
90 **calculation of temperature gradients**

91 Alkenone-derived SSTs from core-top samples virtually identical to the modern
92 annual mean SST at the study site (18.2°C; Locarnini et al. 2019) supported the
93 interpretation that the UK37' SST record at Site U1313 reflected mean annual sea-surface
94 temperatures (Naafs et al., 2012). However, water column and satellite data indicate that
95 most coccolithophorid productivity in subpolar ocean regions occurs from summer to
96 early autumn (Samtleben and Bickert, 1990), biasing alkenone-based SSTs to warm
97 (summer) conditions in locations with surface temperatures below ~15°C (Rosell-Melé et
98 al., 1995). During the time span discussed here, SSTs from Site U1313 dipped below this
99 threshold during cold glacial stages MIS 34, 32, 24, 22, 20 and 16, suggesting that during
100 these periods, SSTs may have been overestimated. Comparison with SSTs based on
101 planktic foraminiferal assemblages at the same location as Site U1313 (Site V30-97,
102 Ruddiman et al., 1989) is supportive of this interpretation as $U^{K_{37}'}$ -based temperatures
103 overlap with summer SSTs estimates during the Last Glacial Maximum but fall between
104 winter and summer SSTs during the Holocene (see Naafs et al., 2013). Alkenone-based SST
105 estimates from Site 982 (Lawrence et al., 2010) likely present a summer-biased
106 temperature throughout the Pleistocene. Indeed, the core-top SST estimate (13°C,
107 Lawrence et al., 2010) fell in the upper range of the modern annual variability (9–13°C)
108 further supporting the assumption of a warm-season bias. The input of allochthonous
109 alkenones likely did not significantly affect alkenone records at U1313 (Naafs et al., 2012),
110 but this bias has been shown to be more significant at higher latitudes or at sites located
111 on or close to continental margins (Mollenhauer et al., 2005). It is not possible to assess

112 the potential influence of allochthonous alkenones in the SST record of Site 982. Apart
113 from this possibility, as alkenones from both sites reflect similar biases when annual mean
114 SSTs at U1313 are cold, the SST gradient between sites U1313 and 982 should be robust
115 during the crucial periods discussed in the text (MIS 24, 22 and 20). During interglacials,
116 the SST gradient may be considered a minimum estimate because alkenone-SSTs at Site
117 U1313 are likely reflecting annual mean (above ~15°C) while Site 982 alkenone-SSTs are
118 summer-biased. Despite these caveats, we infer that $\Delta\text{SST}_{\text{U1313-982}}$ is a faithful
119 representation of heat transport into the high-latitude North Atlantic, particularly during
120 glacial times, which is crucial for this study.

121 Subsurface temperatures from *G. crassaformis*, on the other hand, are unlikely to
122 show seasonal biases because the oxygen-depleted niche preferred by this species is
123 stable below the seasonal thermocline depth (see section 2 of the main text). It is possible
124 that the depth occupied by *G. crassaformis* was influenced by changes in the depth of the
125 pycnocline and/or the shallow oxygen minimum at Site U1313 (cf. section 2). However, we
126 infer that the amplitude of shifts in the calcification depth were relatively minor, as
127 abundant proxy records testify for *G. crassaformis* being a reliable recorder of deep
128 thermocline properties with a stable habitat (e.g., Bahr et al., 2011; Bolton et al., 2018; Karas
129 et al., 2017).

130

131 **S4. Calculation of temperature gradients**

132 Upper ocean stratification was qualitatively estimated using the temperature
133 gradient between alkenone-based SST and Mg/Ca-based SubT at Site U1313. Both records
134 were produced from the same core sections of the primary splice. The age model of Site
135 U1313 was updated as described in section S2. As the temporal resolution of the SST
136 record (1 data point every ~0.6 kyrs) is double than that of SubT (1 data point every ~1.2
137 kyrs), SSTs were linearly interpolated to match SubTs in age (thereby reducing the SST
138 resolution in half). We then subtracted SubT from SST. A similar procedure was followed
139 to calculate the surface temperature gradients between sites U1313 and 982. The age
140 models of both records were produced by tuning benthic oxygen isotopes to the LR04
141 stack. As the temporal resolution of the SST record from Site U1313 is higher than that
142 from Site 982, U1313 SSTs were linearly interpolated to match 982 SSTs in age. We then
143 subtracted 982 SSTs from U1313 SSTs. Both temperature gradients are available in the
144 supplementary data file and PANGAEA database along respective core depths and ages.

145

146 **S5. Relationship between of aridity in the Eastern Mediterranean and** 147 **Mediterranean Outflow Water formation.**

148 Paleo-records from the Eastern Mediterranean realm unanimously point at a high
149 aridity and weak North African monsoon between MIS 25 and 17, promoting the formation
150 of MOW (see main text). This evidence is based on high Isothermal Remanent
151 Magnetization (IRM) at ODP Site 967 (Fig. S8a) indicating increased hematite
152 concentration and inferred to represent enhanced Saharan dust supply (*Larrasoaña et al.*,
153 2003). As dust input reflects wet and arid cycles in the Sahara (*Trauth et al.*, 2009) and

154 annual moisture availability in this region is related to intensity of the African Monsoon,
155 increased IRM indicates a weakened North African monsoonal system, which would allow
156 for increased dust formation and transport to the Eastern Mediterranean. High
157 sedimentary Ti/Al ratios (Fig. S8b, *Konijnendijk et al., 2014*) further support increased dust
158 transport to the Eastern Mediterranean and/or dryness in Northern Africa during this
159 critical interval. These extremely dry conditions in North African and Eastern
160 Mediterranean between MIS 25-17 indicated by these two different proxies (IRM and Ti/Al)
161 are in agreement with a gradual southward shift of the Intertropical Convergence Zone
162 (ITCZ) after ~950 ka (*Trauth et al., 2005; Sepulcre et al., 2011; Seo et al., 2015; Robinson et*
163 *al., 2019*). As the production of MOW strongly depends on the freshwater deficit in the
164 Eastern Mediterranean Sea (which is inversely related to the strength of the North African
165 Monsoon, *Bahr et al., 2015*), the overall aridity increase would favor increased rates of
166 MOW formation from ~930 ka onwards.

167 To further investigate if deep convection in the Eastern Mediterranean promoted
168 enhanced MOW production during the MPT, we developed an Eastern Mediterranean
169 bottom-water density proxy by computing the $\delta^{18}\text{O}$ gradient ($\Delta\delta^{18}\text{O}_{\text{LR04-967}}$) between Site
170 967 in the Eastern Mediterranean (*Konijnendijk et al., 2015*) and the LR04 benthic stack
171 (*Lisiecki and Raymo, 2005, Fig. S8c*). This approach follows the rationale that a denser
172 Eastern Mediterranean bottom-water would indicate strong convection and hence
173 enhanced formation of MOW (*Kaboth et al., 2017*). Considering that both $\delta^{18}\text{O}$ signals
174 record contemporaneous global ice-volume changes, the difference between these
175 oxygen-isotope signals represents a competition between differential responses to salinity
176 and temperature changes at either the Eastern Mediterranean or the global ocean. $\delta^{18}\text{O}$
177 of the LR04 stack is always higher (by 1.2‰ on average) than $\delta^{18}\text{O}$ of Site 967 due to the
178 much colder temperatures at the ocean bottom (modern average ~2°C) in relationship to
179 the Eastern Mediterranean seafloor (modern temperature ~13°C). Between MIS 25 and 17
180 (930–700 ka), contemporaneously to extremely dry conditions in Northern Africa,
181 $\Delta\delta^{18}\text{O}_{\text{LR04-967}}$ decreases, reaching zero around 900 ka. Such an extremely low difference
182 between the LR04 stack and Site 967 indicates a relative increase in salinity and/or
183 decrease in temperature at the latter site, leading to heavier $\delta^{18}\text{O}$ values in eastern
184 Mediterranean that converged to the higher values of the LR04 stack. As both, salinity
185 increase and/or temperature decrease, would increase bottom water densities at Site 967
186 we infer intense deep convection in the Eastern Mediterranean around 900 ka. Increased
187 deep convection would have sustained the production of a dense water mass that
188 occupied the Eastern Mediterranean's seafloor and therefore fostered a strong MOW
189 production between MIS 25 and 17. Enhanced deep convection within the Eastern
190 Mediterranean during this time period is also consistent with the scarcity of sapropels
191 during this time period, because of the overall drier conditions in North Africa and
192 sustained ventilation of the seafloor (*Konijnendijk et al., 2014*).

193 Based on the consistency of the different proxy records discussed above we hence
194 infer that between 950 and 700 ka a weak North African Monsoon enabled sustained deep
195 convection within the Eastern Mediterranean basin and hence fostered strong MOW
196 production throughout this time interval.

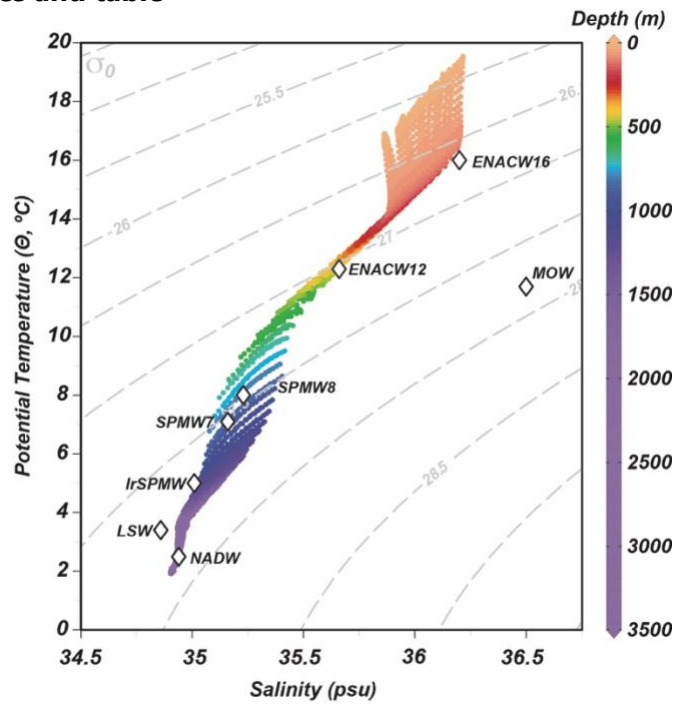
197

198 **S6. Model description and experimental design**

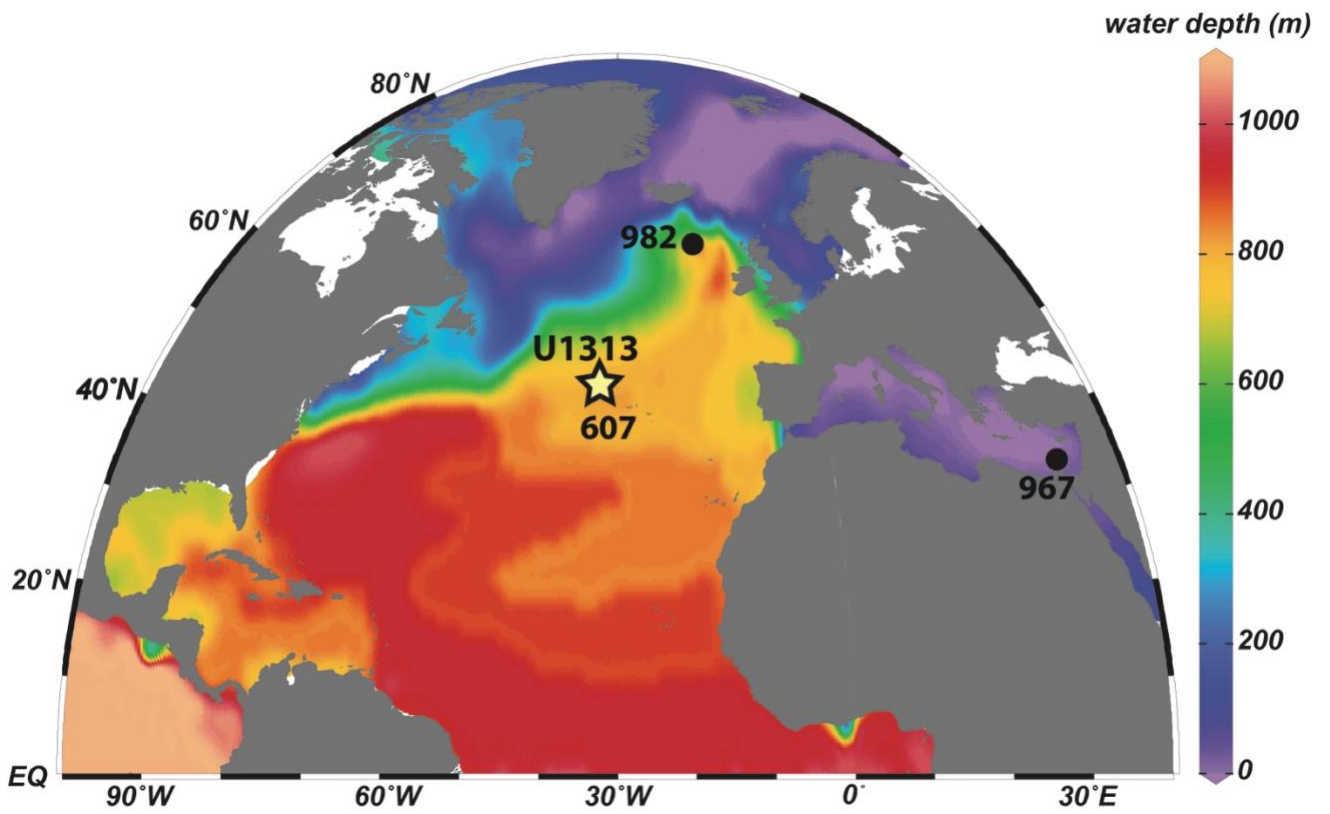
199 We use an Atmosphere General Circulation Model (AGCM), ECHAM5 (*Roeckner et al.*, 2003), to quantify the contributions of the preferential warming of NENA on the mass
200 balance of continental ice sheets in the Atlantic realm during glacial periods. We first
201 conducted a control experiment (A_CTL) by applying boundary conditions (including ice-
202 sheet configurations, greenhouse gases, orbital parameters etc.) and sea-surface forcing
203 (i.e., sea-surface temperature, SST, and sea-ice concentration, SIC) from a glacial
204 experiment (NHIS_0.3s) done by a fully coupled atmosphere-ocean model (AOGCM,
205 *Zhang et al.*, 2014). The prescribed global ice volume in NHIS_0.3s equals a ~50 m sea-
206 level drop. In NHIS_0.3s, the NENA is characterized by a perennial open water area, while
207 extensive sea-ice cover is simulated in the southern flank of the North Atlantic subpolar
208 gyre (i.e., north of Site U1313, Fig. S9). To investigate impacts of the recorded warming on
209 the ice-sheet mass balance, we conducted a sensitivity experiment (A_WARM) in which
210 only the SST in the NENA perennial open water area in A_CTL is substituted by the SST
211 derived from experiment NHIS_0.5 (*Zhang et al.*, 2014), which is 2°C warmer at NENA than
212 NHIS_0.3s (Fig. S9). This provides a direct evaluation of sole impacts of NENA warming on
213 the ice-sheet mass balance.
214

215 Additional ice-volume growth was calculated based on the precipitation anomaly
216 over the northern hemisphere ice-sheet area ($\text{additional_volume} = \text{NH_ice-sheet_area} * \text{precipitation_anomaly} / \text{ocean_area}$). Calculated estimates are considered conservative
217 because our simulations do not consider the possible positive feedbacks from a growing
218 ice sheet on ocean circulation since a higher ice sheet can strengthen the AMOC, leading
219 to an enhancement of precipitation over the ice-sheet area, further increasing its volume
220 (*Zhang et al.*, 2014).
221
222

223 **Supporting figures and table**



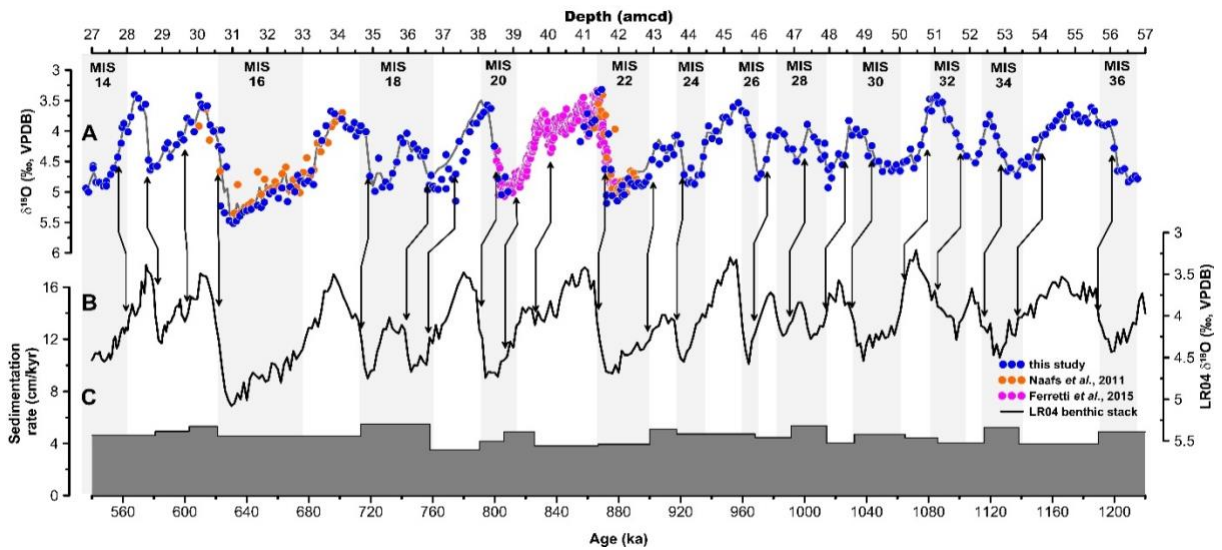
224
225 **Figure S1.** θ-S diagram used to distinguish the water masses at our study site. For this
226 plot we used data from a 10°x10° square centered around the location of Site U1313.
227 Colors represent depth. Diamonds represent the end-members of the water masses as
228 characterized by (García-Ibáñez *et al.*, 2018). ENACW₁₆ and ENACW₁₂ are the Eastern North
229 Atlantic Central Waters of 16°C and 12°C, respectively. SPMW₈ and SPMW₇ are the
230 Subpolar Mode Waters of 8°C, 7°C and Irminger Seas, respectively. LSW= Labrador Sea
231 Water, NADW= North Atlantic Deep Water. MOW is the Mediterranean Outflow close to
232 Cape St. Vincent (Baringer and Price, 1999).
233
234



235
 236
 237
 238
 239
 240

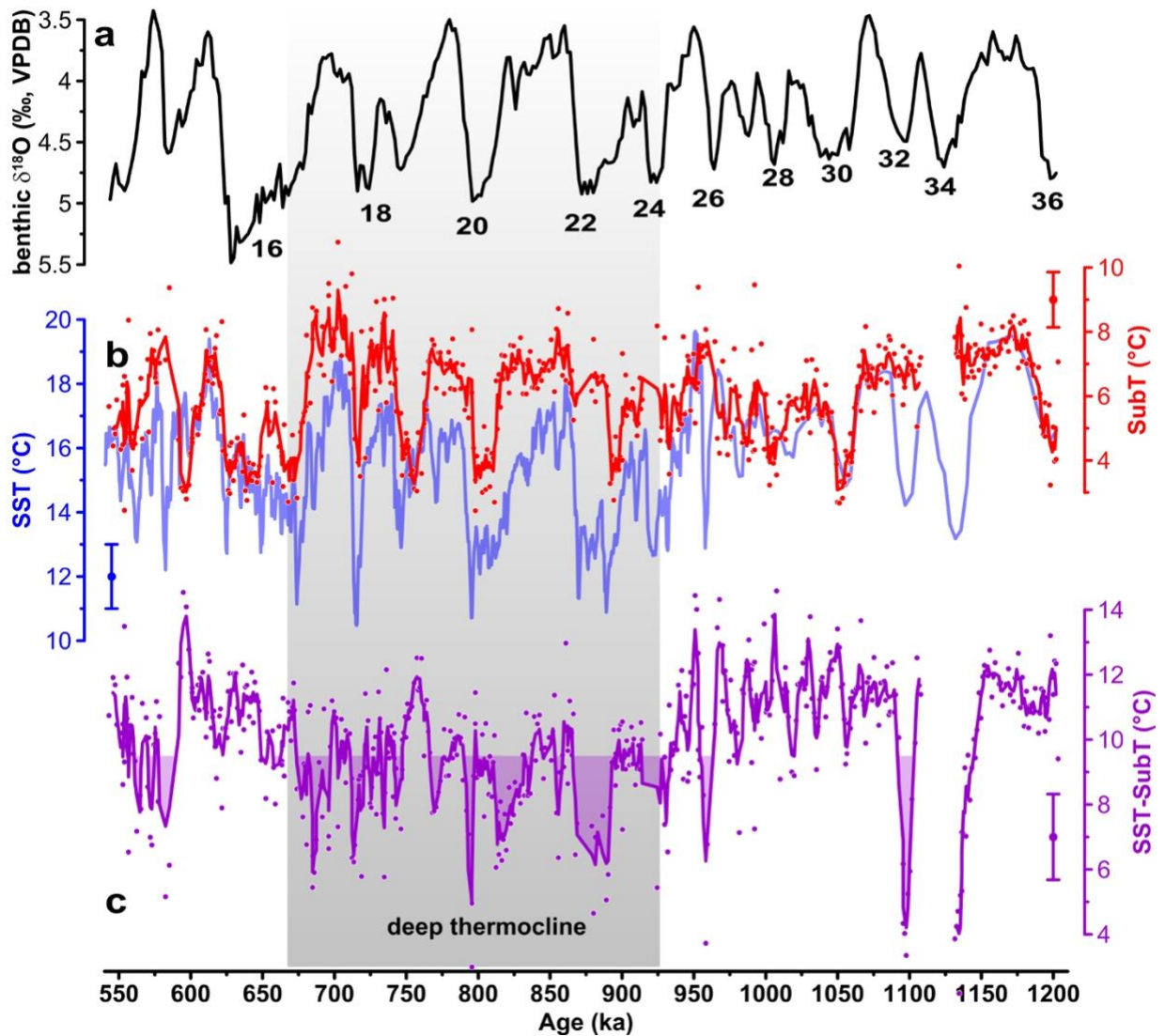
Figure S2. Depth of the isopycnal layer currently located at 800m water depth at Site U1313 across the North Atlantic. Depth of the potential density anomaly layer (isopycnal) $\sigma_0 = 27.45$, located at 800 m water depth at Site U1313.

241



242

243 **Figure S3.** Updated chronostratigraphy of Site U1313 between MIS 36 and 14. (A) Benthic
244 $\delta^{18}\text{O}$ data for Site U1313 on the amcd depth scale (Naafs et al., 2012). Orange circles
245 represent data from Naafs et al., (2011), pink circles from Ferretti et al. (2015), and blue
246 circles represent data produced for this study. The black line represents the resampling
247 every 0.09 m (amcd). (B) LR04 benthic $\delta^{18}\text{O}$ stack (Lisiecki and Raymo, 2005) used as tuning
248 target. Tie points (Table S1) are illustrated by arrows. (C) Sedimentation rate for Site U1313
249 in cm/kyr. Grey bars represent MIS stages according to Lisiecki and Raymo (2005).
250



252

253

254

255

256

257

258

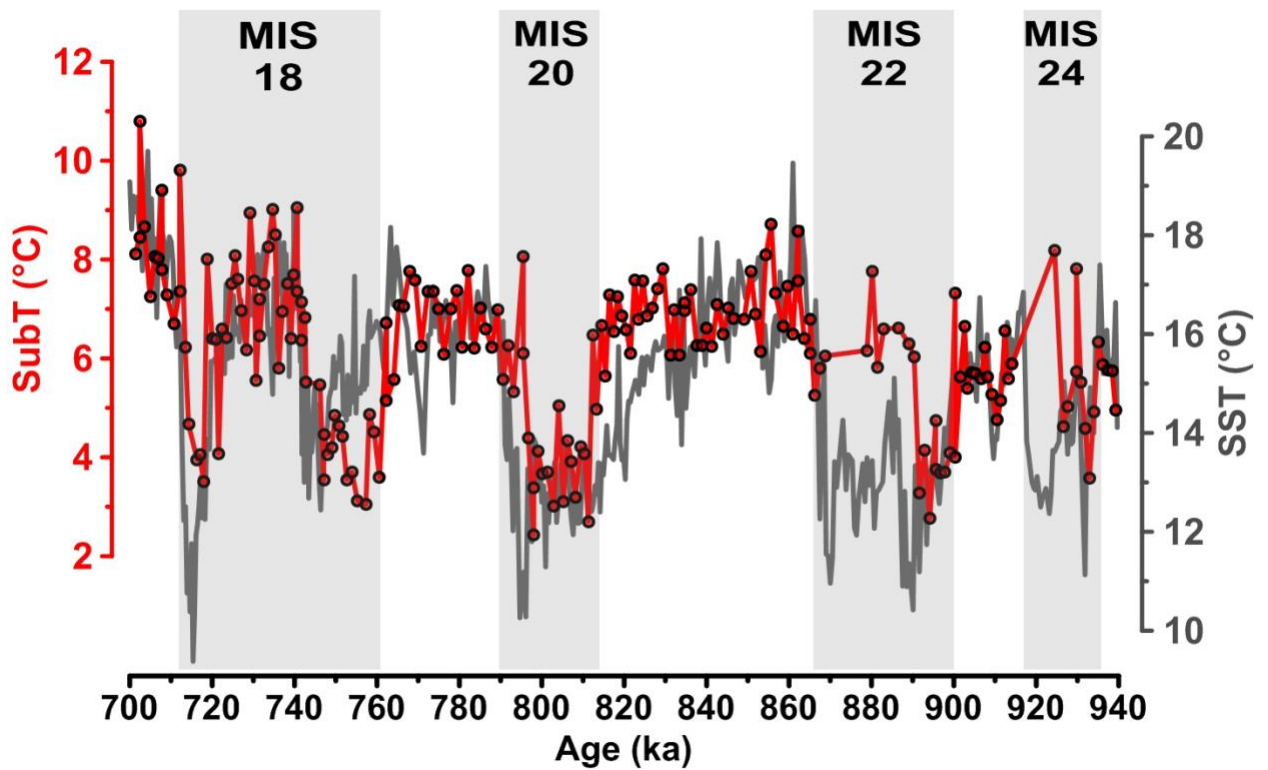
259

260

261

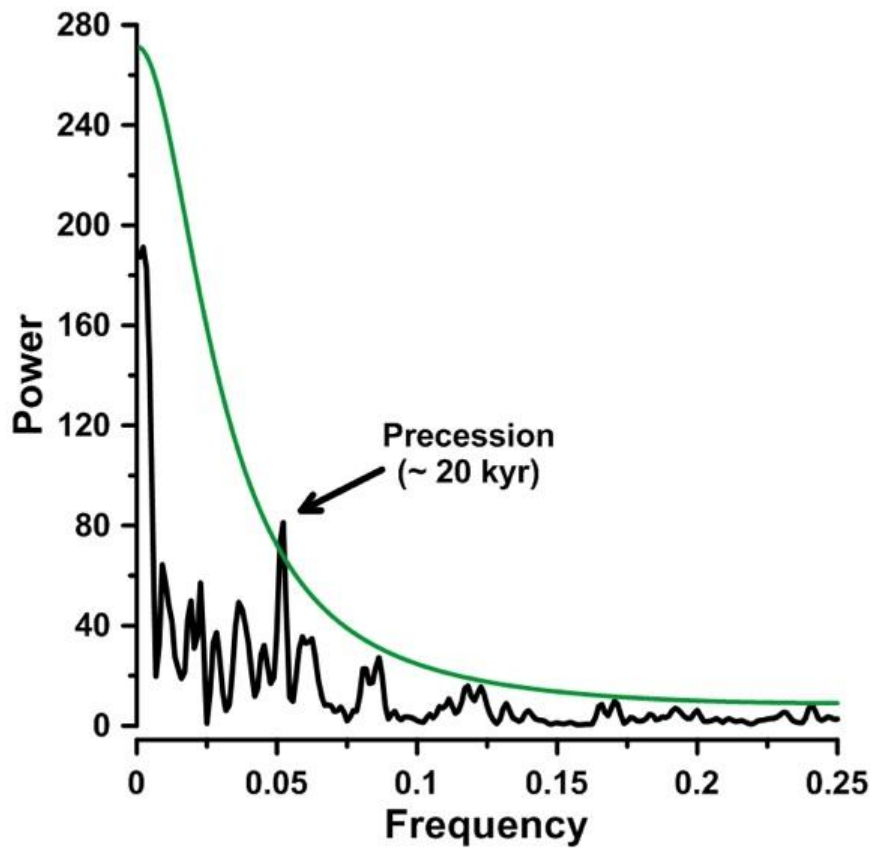
262

Figure S4. (a) U1313 benthic $\delta^{18}\text{O}$ record (this study and (Ferretti *et al.*, 2015), and numbered cold Marine Isotope Stages (Lisiecki and Raymo, 2005). (b) Alkenone-based sea-surface temperatures (Naafs *et al.*, 2012, SST, blue) and Mg/Ca-based subsurface temperatures (SubT, red, this study). (c) Thermocline temperature gradient (SST-SubT). Light purple filling in panel "c" marks temperature-gradient lower than the modern annual average ($\sim 9.5^\circ\text{C}$, Locarnini *et al.*, 2018). Grey box demarks period of long-term weakening of upper-ocean temperature gradient ("stratification") as indicated by low SST-SubT. **Data in panels (b) and (c) were smoothed by 3pt running averages.**



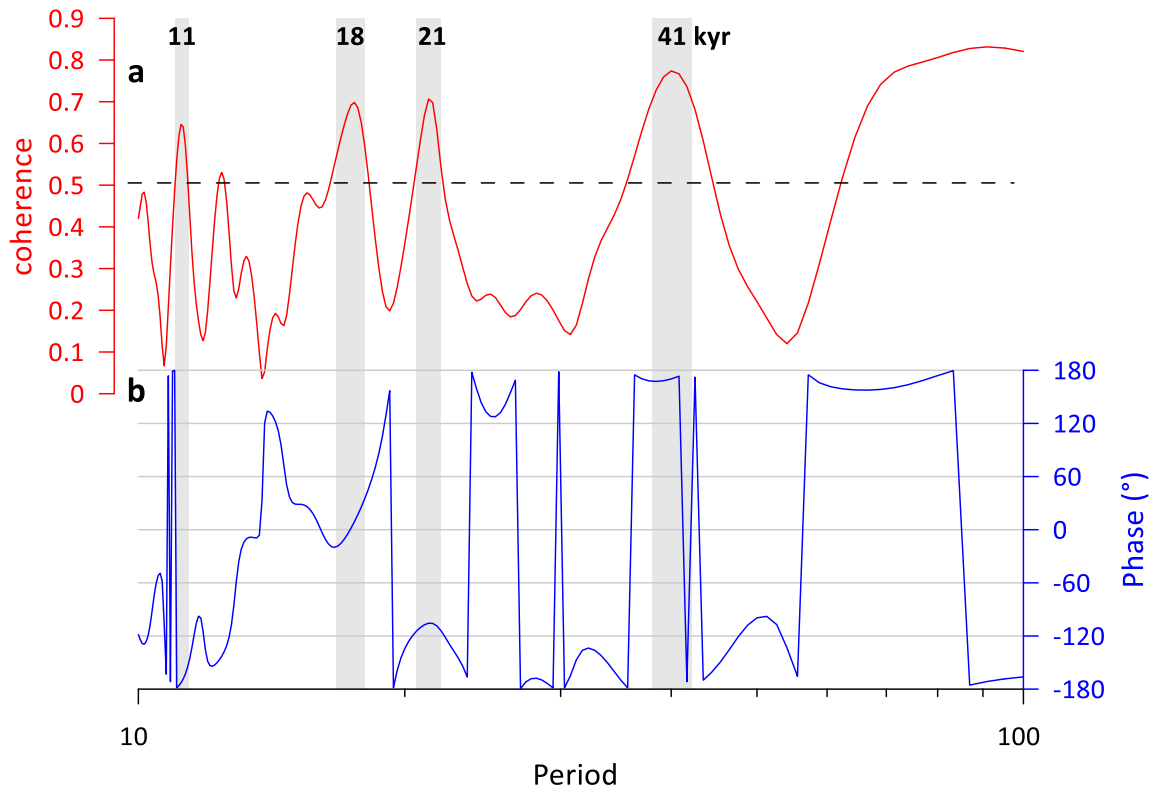
263
 264
 265
 266
 267
 268
 269
 270

Figure S5. Comparison between SST and SubT at Site U1313 between MIS 24 and MIS 18. Mg/Ca-based subsurface temperatures (red line and circles) and alkenone-based SST (grey line). Light gray rectangles denote cold MISs (*Lisiecki and Raymo, 2005*). Both SST and SubT records were produced from the primary splice from Site U1313 and are plotted using the same updated age model, thus avoiding stratigraphic uncertainties.

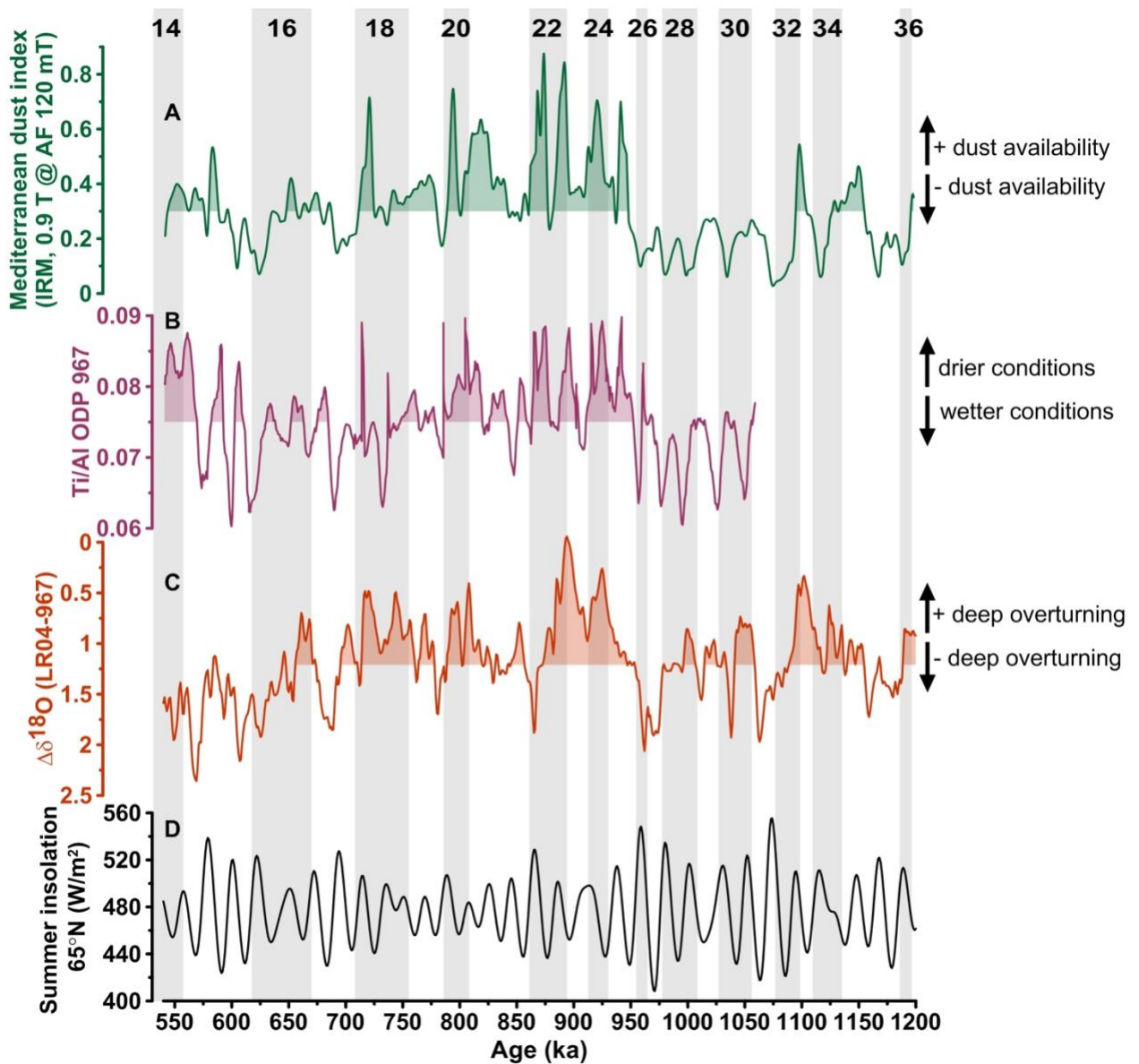


272 **Figure S6.** Power spectrum of our stratification record (SST-SubT). Computed with the
273 interpolated and detrended data using the program REDFIT (*Schulz and Mudelsee, 2002*)
274 implemented in the software PAST (version 3.18, *Hammer et al., 2001*) . The green line
275 marks the 99% chi squared confidence limit.
276

277
278

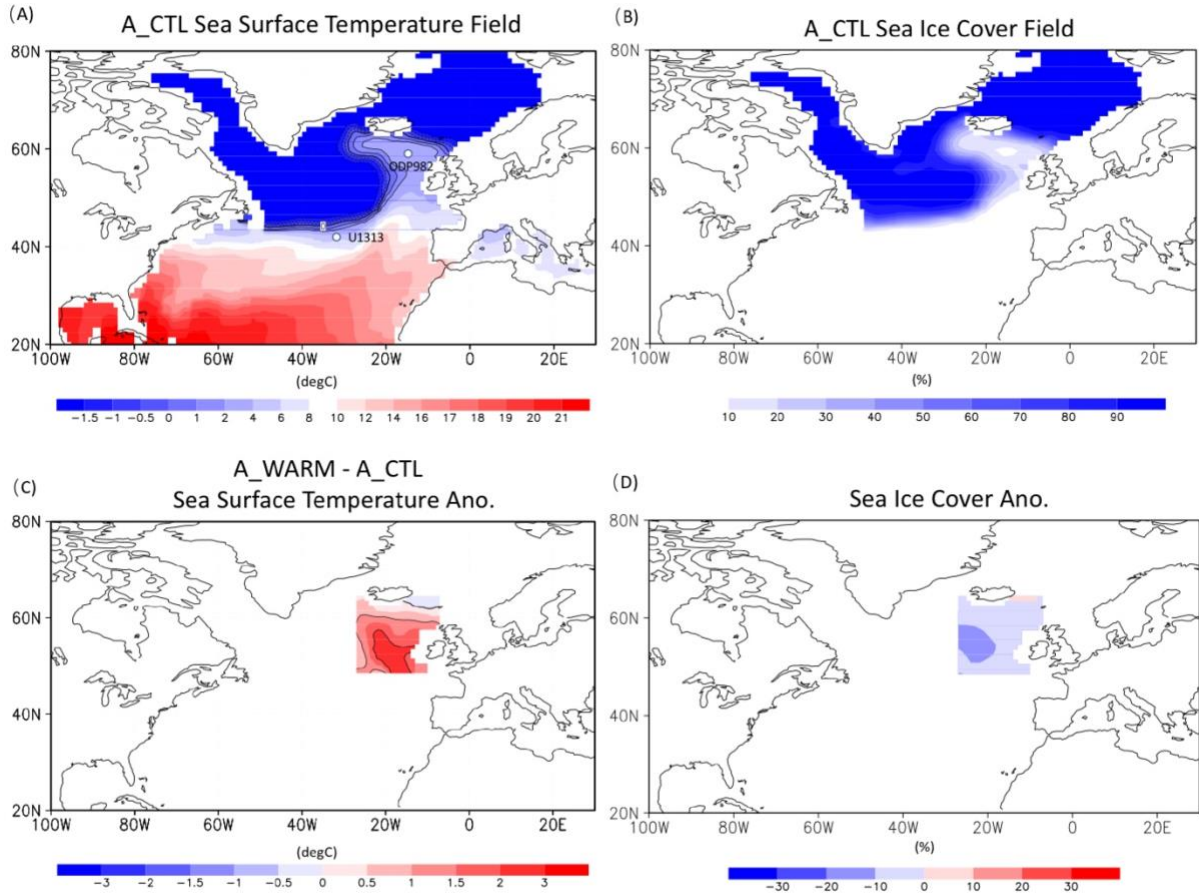


279
280 **Figure S7.** Blackman-Tukey cross spectrum of the Mediterranean dust index at Site 967
281 (Larrasoaña et al., 2003) vs. $\Delta(\text{SST-SubT})$ at Site U1313 based on 2 kyr interpolated and
282 detrended data (performed with AnalySeries v. 2.0.8; Paillard, 2011). (A) Coherence (dashed
283 line indicates 90% confidence level) and (B) phase relation (positive: dust index leads
284 $\Delta(\text{SST-SubT})$). Grey bars indicate significant peaks in the power spectrum with period in
285 kyr. Note the distinct presence of half-precession (11 kyr), precession (18 and 21 kyr), and
286 obliquity (41 kyr)-related periods. Phase lags are close to 180° , as expected from the anti-
287 correlation between strong dust input and weak stratification at Site U1313 (see main text).
288 In-phase coherence for the 18 kyr cycle (in opposition with the ca. -120° phase shift in the
289 21 kyr period) might derive from intermitted offsets between the respective stratigraphies.
290



292
 293
 294
 295
 296
 297
 298
 299

Figure S8. (A) Dust influx into the Eastern Mediterranean Sea derived from isothermal remanent magnetization (*Larrasoña et al., 2003*) (IRM, 0.9 T @ AF 120 mT). (B) Ti/Al at Site 967, derived from XRF core scanning (*Konijnendijk et al., 2014*). (C) Difference between the LR04 global benthic $\delta^{18}\text{O}$ stack (*Lisiecki and Raymo, 2005*) and the benthic $\delta^{18}\text{O}$ values of ODP Site 967 (*Konijnendijk et al., 2015*), used as an approximation for bottom-water density in the Eastern Mediterranean. (D) Summer insolation at 65°N (*Laskar et al., 2004*).



300
 301
 302
 303
 304
 305
 306

Figure S9. Winter sea-surface forcing derived from the modeling experiments. (A) sea-surface temperature (units: °C) and (B) sea-ice concentration in the control experiment A_CTL/NHIS_0.3s. Contours in (A) represent isothermal lines of -1.5, -1, -0.5, 0, 1, and 2. (C) Sea-surface temperature (units: °C) and (D) sea-ice cover anomalies between A_CTL and A_WARM.

Depth adj mcd [amcd]	Depth comp [mcd-top]	Age (ka)
27.84	27.71	562.3
28.63	28.57	580.8
29.76	29.65	602.8
30.67	30.62	621.1
34.86	34.86	713.5
36.39	36.51	743.7
37.21	37.31	758.3
38.47	38.43	790.1
39.13	39.09	805.9
40.10	40.06	825.7
41.68	41.62	866.8
42.94	42.93	900.1
43.80	43.82	917.5
46.21	46.21	968.0
47.26	47.26	991.4
48.48	48.48	1014.2
49.44	49.20	1032.2
50.67	50.74	1064.9
51.68	51.68	1086.1
52.89	52.89	1116.0
54.07	54.06	1138.3
56.10	56.10	1189.7

307
308
309
310
311
312
313
314

Table S1. Tie points between LR04 and updated age model of Site U1313 on the amcd depth scale (*Naafs et al., 2012*).